RSC Advances

PAPER

View Article Online
View Journal | View Issue

Cite this: *RSC Adv.*, 2024, **14**, 32053

Piezoelectric $GaGeX_2$ (X = N, P, and As) semiconductors with Raman activity and high carrier mobility for multifunctional applications: a first-principles simulation

Tuan V. Vu, [ab] Nguyen T. Hiep, [cd] Vo T. Hoa,[e] Chuong V. Nguyen, [f] Huynh V. Phuc, *[g] Bui D. Hoi, [h] A. I. Kartamyshev [ab] and Nguyen N. Hieu *[cd]

In the present work, we propose $GaGeX_2$ (X = N, P, As) monolayers and explore their structural, vibrational, piezoelectric, electronic, and transport characteristics for multifunctional applications based on first-principles simulations. Our analyses of cohesive energy, phonon dispersion spectra, and *ab initio* molecular dynamics simulations indicate that the three proposed structures have good energetic, dynamic, and thermodynamic stabilities. The $GaGeX_2$ are found as piezoelectric materials with high piezoelectric coefficient d_{11} of −1.23 pm V^{-1} for the $GaGeAs_2$ monolayer. Furthermore, the results from electronic band structures show that the $GaGeX_2$ have semiconductor behaviours with moderate bandgap energies. At the Heyd–Scuseria–Ernzerhof level, the $GaGeP_2$ and $GaGeAs_2$ exhibit optimal bandgaps for photovoltaic applications of 1.75 and 1.15 eV, respectively. Moreover, to examine the transport features of the $GaGeX_2$ monolayers, we calculate their carrier mobility. All three investigated $GaGeX_2$ systems have anisotropic carrier mobility in the two in-plane directions for both electrons and holes. Among them, the $GaGeAs_2$ monolayer shows the highest electron mobilities of 2270.17 and 1788.59 $cm^2\ V^{-1}\ s^{-1}$ in the *x* and *y* directions, respectively. With high electron mobility, large piezoelectric coefficient, and moderate bandgap energy, the $GaGeAs_2$ material holds potential applicability for electronic, optoelectronic, piezoelectric, and photovoltaic applications. Thus, our findings not only predict stable $GaGeX_2$ structures but also provide promising materials to apply for multifunctional devices.

Received 5th September 2024
Accepted 1st October 2024

DOI: 10.1039/d4ra06406b

rsc.li/rsc-advances

1 Introduction

The growing demand for clean and renewable energy has stimulated the requirement for new materials and technologies that can generate clean energy to solve the energy crisis and environmental pollution problems. Exploring Janus two-dimensional (2D) materials has opened more opportunities for developing high-efficiency energy conversion techniques. Due to the asymmetric structures, the Janus 2D materials own unique photovoltaic,[1,2] electronic[3,4] catalytic,[5,6] optical,[7] and piezoelectric properties.[8,9] Consequently, some 2D materials of black phosphorus,[10] bismuthene[11] MXenes,[12] metal sulfides,[13,14] and group III chalcogenides[15–17] have shown various application prospects in energy conversion and storage devices. Among them, photovoltaic and piezoelectric technologies are potential approaches for clean and renewable energy sources.

Based on the above reasons, some research groups have explored and demonstrated the Janus materials for high-performance photovoltaic devices. Bouziani *et al.* proposed Janus Sn_2SSe and $SnGeS_2$ monolayers for ultra-thin solar cells. These tin monochalcogenides showed indirect semiconductor behaviours with optimal bandgap energies of about 1.60 eV. The monolayers also possessed the highest optical conductivity and absorption coefficient of 4513 $\Omega^{-1}\ cm^{-1}$ and 63.5 μm^{-1}, respectively. The solar cells based on the Sn_2SSe and $SnGeS_2$ nano-sheet absorbers reached a high conversion efficiency of 28.12% and 27.47%, respectively. These results revealed that the tin monochalcogenides were promising candidates for next-

[a]*Laboratory for Computational Physics, Institute for Computational Science and Artificial Intelligence, Van Lang University, Ho Chi Minh City, Vietnam. E-mail: tuan.vu@vlu.edu.vn*

[b]*Faculty of Mechanical – Electrical and Computer Engineering, School of Technology, Van Lang University, Ho Chi Minh City, Vietnam*

[c]*Institute of Research and Development, Duy Tan University, Da Nang 550000, Vietnam. E-mail: hieunn@duytan.edu.vn*

[d]*Faculty of Natural Sciences, Duy Tan University, Da Nang 550000, Vietnam*

[e]*Department of Scientific Management and International Cooperation, Quang Nam University, Quang Nam, Vietnam*

[f]*Department of Materials Science and Engineering, Le Quy Don Technical University, Hanoi 100000, Vietnam*

[g]*Division of Physics, School of Education, Dong Thap University, Cao Lanh 870000, Vietnam. E-mail: hvphuc@dthu.edu.vn*

[h]*Department of Physics, University of Education, Hue Unversity, Hue, Vietnam*

generation photovoltaic technology.[18] Janus MoA_2Z_4 monolayers with A = Si/Ge, Z = N/P/As were found to have outstanding catalytic and photovoltaic performances by using the first principles computations. The MoA_2Z_4 monolayers were stable semiconductors with good mechanical properties and favorable bandgap energies of 0.69 to 2.44 eV for absorption in the visible region. From the small effective mass or large elastic modulus, the MoA_2Z_4 exhibited high carrier mobility up to 10^3 to 10^4 cm^2 V^{-1} s^{-1}. Moreover, their electronic band structures were tunable by applying strain.[19] Wang and co-workers studied optical and electronic characteristics of Janus Ga_2SeTe based on first principles investigations. They found that the Ga_2SeTe had direct bandgap and high optical absorption with ultrafast charge separation. The solar cell devices based on Ga_2SeTe absorber exhibited high conversion efficiency up to 19.0%. This indicated the potential feasibility of the Janus Ga_2SeTe materials for thin film solar cell applications.[20] In addition, some Janus materials also possessed excellent piezoelectric effects to apply in piezoelectric technology which used mechanical energy to produce electricity and *vice versa*. For instance, Janus transition metal dichacolgenides of MXY with X/Y = S, Se, Te and M = Mo, W showed strong piezoelectric effects based on *ab initio* calculations. By applying a uniaxial strain, both in-plane as well as additional out-of-plane polarizations were induced. The MoSTe exhibited a large out-of-plane piezoelectric coefficient d_{33} up to 13.5 pm V^{-1} which was higher than the commonly used AlN piezoelectric material (d_{33} = 5.6 pm V^{-1}).[21] Janus Ga_2XY with X/Y = O, S, Se, and Te monolayers were found as piezoelectric semiconductors. From the first-principles simulations, the monolayers showed mechanical, dynamic, and thermodynamic stabilities with bandgap values of 1.00 to 3.24 eV. These monolayers exhibited high in-plane coefficients ranging from 3.09 to 5.67 pm V^{-1} as well as extra out-of-plane piezoelectric coefficients of 0.11 to 0.34 pm V^{-1}. Notably, distinctive properties were observed for O-participated monolayers with more stable structures, lower bandgaps, and reversed dipole direction from O to S/Se. The results revealed that the Ga_2XY could be promising candidates for piezoelectric and optoelectronic devices.[22]

For applications in multifunctional devices, the efficient transport properties with high carrier mobility of the materials are an important factor. Therefore, besides the moderate bandgaps and large piezoelectric coefficients, the Janus materials with high carrier mobility are also attracting more interest for applications in the electronic field. Thus, in this work, we construct the $GaGeX_2$ monolayers with X = N/P/As and investigate their fundamental characteristics for multifunctional applications based on the first-principles investigations. The crystal stabilities are examined by the phonon dispersions and simulations of *ab initio* molecular dynamics. We also perform Raman spectra for the Raman activities and vibrational properties of the $GaGeX_2$ systems. The piezoelectric coefficients of all three monolayers are calculated to evaluate the piezoelectric effects. The electronic band structures are studied by using the Perdew–Burke–Ernzerhof (PBE) as well as Heyd–Scuseria–Ernzerhof (HSE06) investigations. To elucidate the transport properties of the $GaGeX_2$ monolayers, we estimate the mobility of carriers from their effective masses, elastic modulus, and deformation potential constants.

2 Computational details

The density functional theory (DFT) investigations in this work were carried out within the Vienna *ab initio* simulation program.[23,24] The projector-augmented wave method was used to treat the interaction between ions and valence electrons.[25,26] The exchange–correlation functional was solved within the generalized gradient approximation of PBE.[27] The unit cell of the monolayers was relaxed with a *k*-point grid of 12 × 12 × 1 in the first Brillouin zone (BZ). The PHONOPY package was used in a unit cell of 4 × 4 × 1 with the finite displacement technique for phonon spectra.[28] To calculate the electronic band structures, we employed the hybrid functional of HSE06 with the spin-orbital coupling (SOC).[29] The *ab initio* molecular dynamics (AIMD) calculation was performed at 10 ps at room temperature for the thermal stability of the systems. The semi-empirical DFT-D3 method was conducted to examine the van der Waals forces.[30] The total energy convergence criteria of 10^{-6} eV was employed for electronic relaxation. We set the Hellmann–Feynman forces of 10^{-3} eV $Å^{-1}$ to optimize the structures. A vacuum space of 30 Å and a cut-off energy of 600 eV were used. The Bader technique was conducted for the distribution of charge. We calculated the macroscopic dielectric tensors for Raman responses and piezoelectric/elastic coefficients by using the finite displacement technique and density functional perturbation theory (DFPT), respectively.[31] The effective mass and mobility of carriers were estimated by the deformation potential (DP) method for the transport properties.[32]

3 Results and discussion

3.1 Crystal structure and stability

Firstly, we design and optimize the crystal structures of the $GaGeX_2$ monolayers. Fig. 1(a) depicts the top and side views of the $GaGeX_2$ structures with the black rhombus unit-cell. The monolayers have hexagonal geometry with a symmetry group of D_{3h} as seen from the top view. The side view of the $GaGeX_2$ monolayers shows that their crystal structures are composed by stacking in order eight atomic layers of X–Ge–X–Ga–Ga–X–Ge–X, forming a symmetric structure to the horizontal plane between the two Ga atoms. The optimized lattice constants are determined to be 3.12 Å for $GaGeN_2$, 3.75 Å for $GaGeP_2$, and 3.92 Å for $GaGeAs_2$ monolayer. The calculated bond lengths (d) and thicknesses (h) of the configurations are also listed in Table 1. Due to the increases in bond lengths between atoms, the h values increase from 9.02 Å for $GaGeN_2$ to 11.40 Å for $GaGeAs_2$. When the X element increases atomic radius from N to P and As, both the lattice constants and thicknesses of the $GaGeX_2$ monolayers gradually increase. This increasing trend has also observed in other reported $ZrGeN_3H$, $ZrGeP_3H$, and $ZrGeAs_3H$ Janus structures.[33]

We then calculate the cohesive energy (E_{coh}) which represents the bonding strength of atoms within the solid by using the following formula:

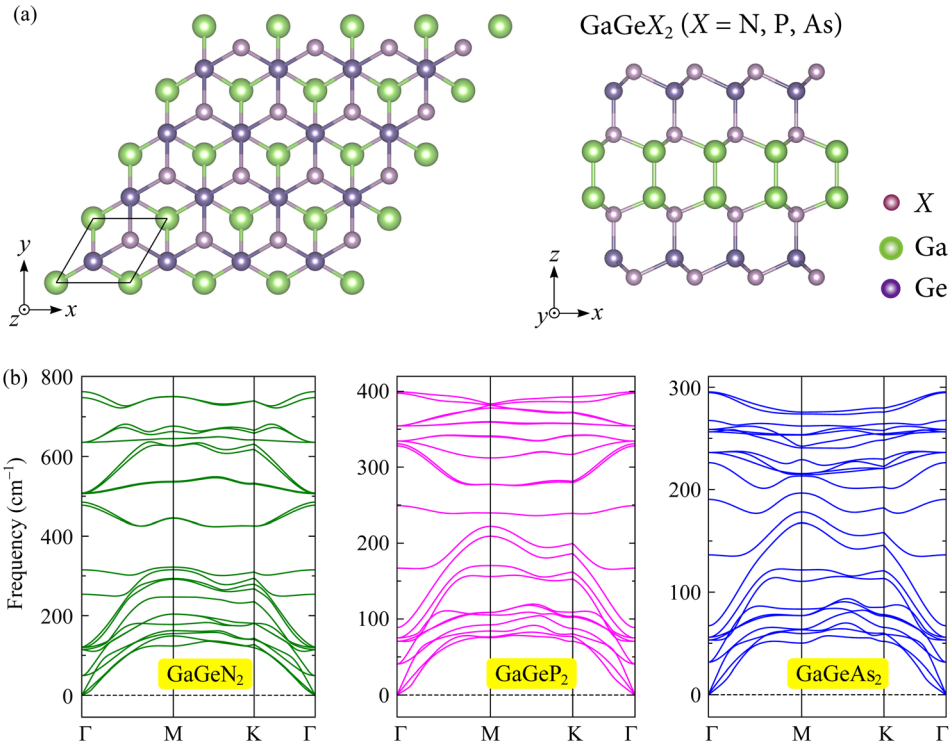

Fig. 1 (a) Crystal structure (top and side views) and (b) phonon dispersions of $GaGeX_2$ (X = N/P/As) monolayers.

$$E_{coh} = \frac{(2E_{Ga} + 2E_{Ge} + 4E_X) - E_{tot}}{N_{tot}}, \quad (1)$$

Here E_{tot} indicates the total energy of the $GaGeX_2$ monolayers and N_{tot} refers the total atom number in the unit cell ($N_{tot} = 8$). E_{Ga}, E_{Ge}, and E_X are the energy of Ga, Ge, and X atoms, respectively.

The calculated E_{coh} values are presented Table 1. The positive and high E_{coh} values of the $GaGeX_2$ monolayers suggest the high energetic stability of these systems. Among them, the $GaGeN_2$ monolayer shows the highest cohesive energy of 7.69 eV per atom, while the $GaGeP_2$ and $GaGeAs_2$ have lower E_{coh} of 5.72 and 5.24 eV per atom, respectively. The high E_{coh} of $GaGeN_2$ is due to its short bond lengths, leading to stronger chemical bonds of atoms in the $GaGeN_2$ structure.

Moreover, we conduct the phonon dispersions to check the dynamic stability of the $GaGeX_2$ systems. The phonon dispersion results of the monolayers are presented in Fig. 1(b). All three structures have twenty-four phonon branches in the phonon spectra because of the presence of eight atoms in their unit cells. It can be seen that the highest frequency of the phonon dispersions is gradually decreased as the X atom transfers from N to P/As, leading to the compression of the frequency range in the phonon bands. Besides, the intersection of acoustic and optical vibrational modes in the low-frequency ranges causes optical-acoustic scattering with low thermal conductivity. In general, the phonon dispersions of the $GaGeX_2$ monolayers exhibit positive frequencies without the existence of imaginary frequencies over the BZ. This indicates that the $GaGeX_2$ structures are dynamically stable.

Additionally, we perform the AIMD simulations to examine the thermal stability of the $GaGeX_2$ monolayers by heating the structures to 300 K in the duration of 10 ps. The total energy fluctuations during the simulations are depicted in Fig. 2(a). We can observe only small energies change throughout the heating, suggesting that the $GaGeX_2$ structures are thermodynamically stable at room temperature. The electron localization functions (ELF) are also analyzed for the chemical bonding behaviours of the $GaGeX_2$ monolayers. As presented in Fig. 2(b), the red regions for the high probability of electron localization are observed around N, P, and As atoms. Meanwhile, the electron localization is quite low around the Ga and Ge atoms, implying the charges might transfer from Ga and Ge to X atoms.

Table 1 Constant of lattice a (Å), four bond lengths between atoms d (Å), thickness of monolayers h (Å), cohesive energy E_{coh} (eV per atom), PBE/HSE06/HSE + SOC bandgap energies E_g (eV) and work function Φ (eV) of $GaGeX_2$ monolayers

	a	d_{Ga-Ga}	d_{Ga-X}	d_{X-Ge}	d_{Ge-X}	h	E_{coh}	E_g^{PBE}	E_g^{HSE06}	$E_g^{HSE+SOC}$	Φ
$GaGeN_2$	3.12	2.46	1.98	1.88	1.89	9.02	7.69	1.75	2.90	2.89	6.31
$GaGeP_2$	3.75	2.47	2.35	2.33	2.39	10.96	5.72	1.08	1.75	1.70	5.31
$GaGeAs_2$	3.92	2.47	2.45	2.44	2.52	11.40	5.24	0.47	1.15	1.04	4.79

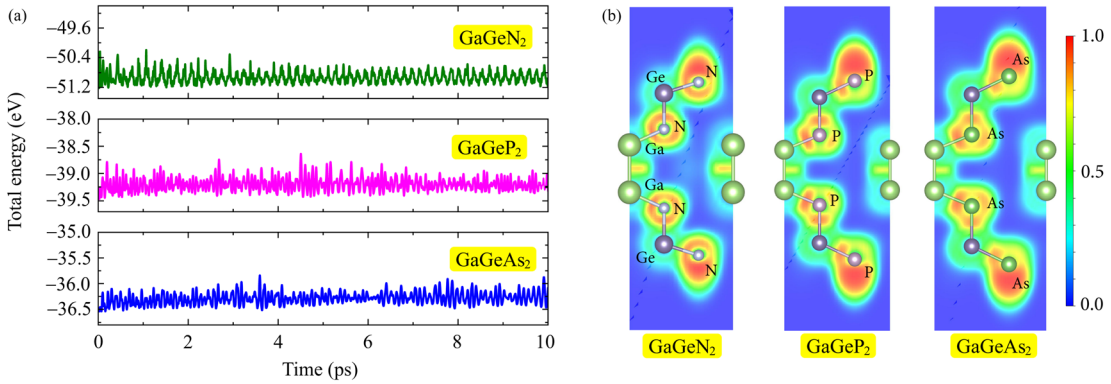

Fig. 2 (a) The total energy-simulation time dependences at 300 K by AIMD calculations and (b) electron localization function (ELF) of $GaGeX_2$ structures. The high–low charge densities are indicated by the red-blue regions.

3.2 Raman active modes and vibrational properties

In this section, we examine the Raman spectra and vibrational properties of the $GaGeX_2$ monolayers. Raman spectroscopy is considered a reliable technique for analyzing physical characteristics such as chemical composition, structural phase, and electronic structure of the materials. For Raman measurement by experiments, a light beam is focused onto the sample, and then we collect the scattered photons to evaluate the shift of light intensity dispersion for Raman responses. Similar to Raman theory, from the interaction of incident photons with molecules in the material, we can obtain Raman scattering. The energy difference of the incident and scattered photons which correlated to the vibrational mode energies can give information about the Raman shift in the Raman spectrum. In this study, we use the finite displacement approach to calculate the Raman activity tensors of phonon modes at Γ-point in the BZ. As mentioned, the $GaGeX_2$ monolayers have the symmetry of D_{3h} point group. The optical modes in the phonon spectra at Γ-point are either doubly degenerate or non-degenerate. The corresponding irreducible representation of the optical modes can be written as $\Gamma = 4E' + 3E'' + 4A_1' + 3A_2''$, with A_1'/A_2'' are non-degenerate out-of-plane vibrations and E'/E'' relate to doubly degenerate in-plane vibrations. Among these vibration modes, A_1', E', and E'' are Raman active modes.

Fig. 3 illustrates the calculated Raman spectra of the $GaGeX_2$ monolayers. We can observe that the Raman spectrum of the $GaGeN_2$ shows five high-intensity peaks at 119, 315, 485, 636, and 763 cm^{-1}, in which the peaks at 315, 485, and 763 cm^{-1} are the A_1' phonon mode. Meanwhile, the main peaks in the Raman spectra of the $GaGeP_2$ $GaGeAs_2$ monolayers are located at 334 cm^{-1} and 238 cm^{-1}, respectively. We can observe the change of the highest intensity peak to the lower frequency when the X element transfers from N to P/As. This correlates to the increase of the atomic mass of X in the $GaGeX_2$ structures.

3.3 Mechanical properties and piezoelectricity

The mechanical and piezoelectric characteristics of the $GaGeX_2$ structures are also analyzed by calculating the mechanical tensors and piezoelectric coefficients. Four different elastic constants require to find are C_{11}, C_{12}, C_{22}, and C_{66}. We have $C_{11} = C_{22}$ due to the hexagonal structures of the $GaGeX_2$. Thus, three elastic constants of C_{11}, C_{12}, and C_{66} are calculated by adding a strain ranging from −1.5 to 1.5% along two in-plane directions and polynomial fitting the energy changing with the applied strain.[34] The attained elastic constants are presented in Table 2. The C_{11}, C_{12}, and C_{66} values vary from 161.89, 42.96, and 59.46 N m^{-1} for $GaGeAs_2$ to 390.78, 118.05, and 136.36 N m^{-1} for $GaGeN_2$, respectively. It can be seen that these positive elastic constants of the three monolayers satisfy the condition of $C_{11} - C_{12} > 0$ according to the criterion of Born–Huang for mechanical stability.[35,36] This demonstrates the mechanically stable $GaGeX_2$ structures for experimental fabrication.

Next, from the obtained elastic constants, we calculate the elastic modulus for the compressive and tensile stiffness of the materials, Young's modulus (Y_{2D}), by using the following formula:

$$Y_{2D} = \frac{C_{11}^2 - C_{12}^2}{C_{11}}. \quad (2)$$

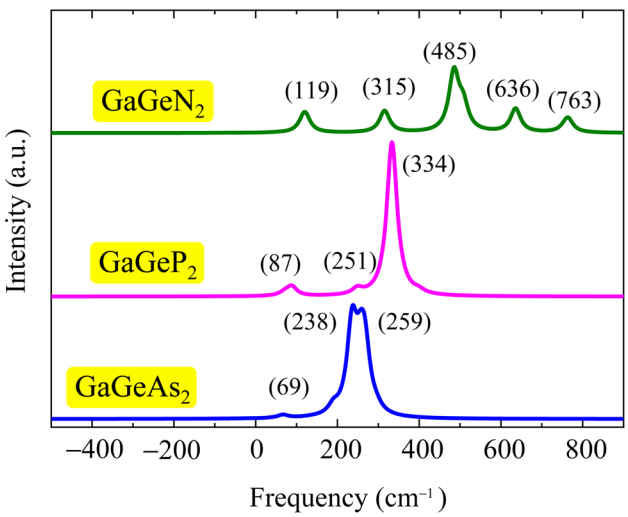

Fig. 3 Calculated Raman spectra of $GaGeN_2$, $GaGeP_2$, and $GaGeAs_2$ monolayers.

Table 2 Three elastic coefficients of C_{11}, C_{12}, C_{66}, Young's modulus Y_{2D}, ratio of Poisson ν and piezoelectric coefficients e_{11}, e_{31}, d_{11}, and d_{31} of $GaGeX_2$ materials

	C_{11} (N m^{-1})	C_{12} (N m^{-1})	C_{66} (N m^{-1})	Y_{2D} (N m^{-1})	ν	e_{11} (10^{-10} C m^{-1})	e_{31} (10^{-10} C m^{-1})	d_{11} (pm V^{-1})	d_{31} (pm V^{-1})
$GaGeN_2$	390.78	118.05	136.36	355.11	0.30	−2.37	0.00	−0.87	0.00
$GaGeP_2$	197.35	49.78	73.78	184.79	0.25	−1.60	0.00	−1.09	0.00
$GaGeAs_2$	161.89	42.96	59.46	150.49	0.27	−1.46	0.00	−1.23	0.00

As listed in Table 2, the attained Y_{2D} values of the $GaGeX_2$ structures vary from 150.49 to 184.79 and 355.11 N m^{-1} for the $GaGeAs_2$, $GaGeP_2$ and $GaGeN_2$, respectively. The decrease of Y_{2D} when X changes from N to P and As is associated with the increase of bond lengths. Since the bond lengths of $GaGeN_2$ are shorter than that of the $GaGeP_2$ and $GaGeAs_2$ monolayers, the $GaGeN_2$ exhibits higher Y_{2D} value. Thus the $GaGeN_2$ is quite stiff, while the $GaGeP_2$ and $GaGeAs_2$ are more flexible and mechanically stable. The Y_{2D} values of the $GaGeP_2$ and $GaGeAs_2$ monolayers are comparable with the reported values of $SMoSiP_2$ (Y_{2D} = 163.48 N m^{-1}),[37] $MoSi_2P_4$ (Y_{2D} = 204.80 N m^{-1}),[38] and $WSiP_3H$ (Y_{2D} = 152.47 N m^{-1}).[39]

In addition, we measure the deformation of materials by calculating the Poisson's ratio ν_{2D} of the $GaGeX_2$ structures. The ν_{2D} is expressed as:

$$\nu_{2D} = \frac{C_{12}}{C_{11}}. \quad (3)$$

The obtained ν_{2D} values are shown in Table 2. The $GaGeX_2$ monolayers show isotropic Poisson's ratios of 0.30 for $GaGeN_2$, 0.25 for $GaGeP_2$, and 0.27 for $GaGeAs_2$. These values are lower than the Poisson's ratios of $ZrSiGeN_4$ (ν_{2D} = 0.34)[40] and Ga_2STe_2 (ν_{2D} = 0.36) monolayers.[16]

For piezoelectric applications, we also investigate the piezoelectric effects of the $GaGeX_2$ monolayers. When we apply a mechanical stress to a piezoelectric material, it will cause a deformation of crystal structure and generate electricity due to the imbalanced electric charge distribution. To have this interesting property, the piezoelectric material must have a noncentrosymmetric lattice structure for the electric dipole generation. The 2D Janus monolayers with anisotropic structures are expected to exhibit not only in-plane piezoelectricity but also extra out-of-plane piezoelectricity. In this work, we use the DFT calculation method reported by Duerloo and coworkers to study the piezoelectric effects of the $GaGeX_2$.[34] By analyzing the polarization changes from the applied mechanical strains, we can estimate the piezoelectric coefficients (e_{ijk} and d_{ijk}) as follows:

$$e_{ijk} = \frac{\partial P_i}{\partial \varepsilon_{jk}}, \quad (4)$$

$$d_{ijk} = \frac{\partial P_i}{\partial \sigma_{jk}}, \quad (5)$$

where (i, j, k) are (1, 2, 3) indicating (x, y, z), respectively. σ_{jk}, ε_{jk}, and P_i refer to the stress, strain, and polarization, respectively.

According to the calculated e_{11} and e_{31} values, the d_{11} and d_{31} are attained by using following formulas:[41]

$$d_{11} = \frac{e_{11}}{C_{11} - C_{12}}, \quad (6)$$

$$d_{31} = \frac{e_{31}}{C_{11} + C_{12}}. \quad (7)$$

Table 2 summarizes the resulting piezoelectric coefficient values. As depicted in Fig. 1(a), the $GaGeX_2$ monolayers have the D_{3h} symmetry, then they exhibit only the in-plane piezoelectric effect. Therefore, the e_{31} and d_{31} values for the out-of-plane coefficients are zero. To determine the piezoelectric coefficient, we calculate the dependence of polarization change on the small uniaxial strains.[34,42] The obtained values are linearly fitted. The relaxed-ion piezoelectric coefficient determined by the slope of the line[43] and the positive or negative value depends on the increasing or decreasing trend of polarization change with uniaxial strain.[34,42] The obtained in-plane piezoelectric coefficients e_{11} and d_{11} for the $GaGeN_2$, $GaGeP_2$, and $GaGeAs_2$ are -2.37×10^{-10} C m^{-1} and −0.87 pm V^{-1}, -1.60×10^{-10} C m^{-1} and −1.09 pm V^{-1}, -1.46×10^{-10} C m^{-1} and −1.23 pm V^{-1}, respectively. Notably, when the X element changes from N to P and As, the absolute values of d_{11} increase. The high absolute d_{11} value of the $GaGeAs_2$ monolayer are comparable with other Janus materials of $WSiN_3H$ (d_{11} = 0.99 pm V^{-1}),[39] $MoSi_2N_4$ (d_{11} = 1.144 pm V^{-1}), and $WSiGeN_4$ (d_{11} = 1.050 pm V^{-1}),[44] making this material suitable for piezoelectric applications.

3.4 Electronic properties

In the following, we examine the electronic properties of the $GaGeX_2$ monolayers by calculating their band structures. As depicted in Fig. 4(a), the electronic structures calculated at the PBE level exhibit semiconductor characteristics for all three $GaGeX_2$ systems. The obtained bandgap values (E_g) are listed in Table 1. The $GaGeN_2$ has the highest E_g of 1.75 eV, while the E_g of $GaGeP_2$ and $GaGeAs_2$ are 1.08 and 0.47 eV, respectively. The $GaGeN_2$ and $GaGeP_2$ are found as indirect semiconductors, while the $GaGeAs_2$ is a direct semiconductor with both conduction and valence band edges located at Γ-point in the BZ. Besides, due to the underestimated bandgap problem, the HSE06 approach is also used for estimating more accurate bandgap values. The electronic bands from the HSE06 method of the $GaGeX_2$ monolayers show similar structures with the electronic bands from the PBE method. However, the calculated bandgap values at the HSE06 level are higher with 2.90 eV for

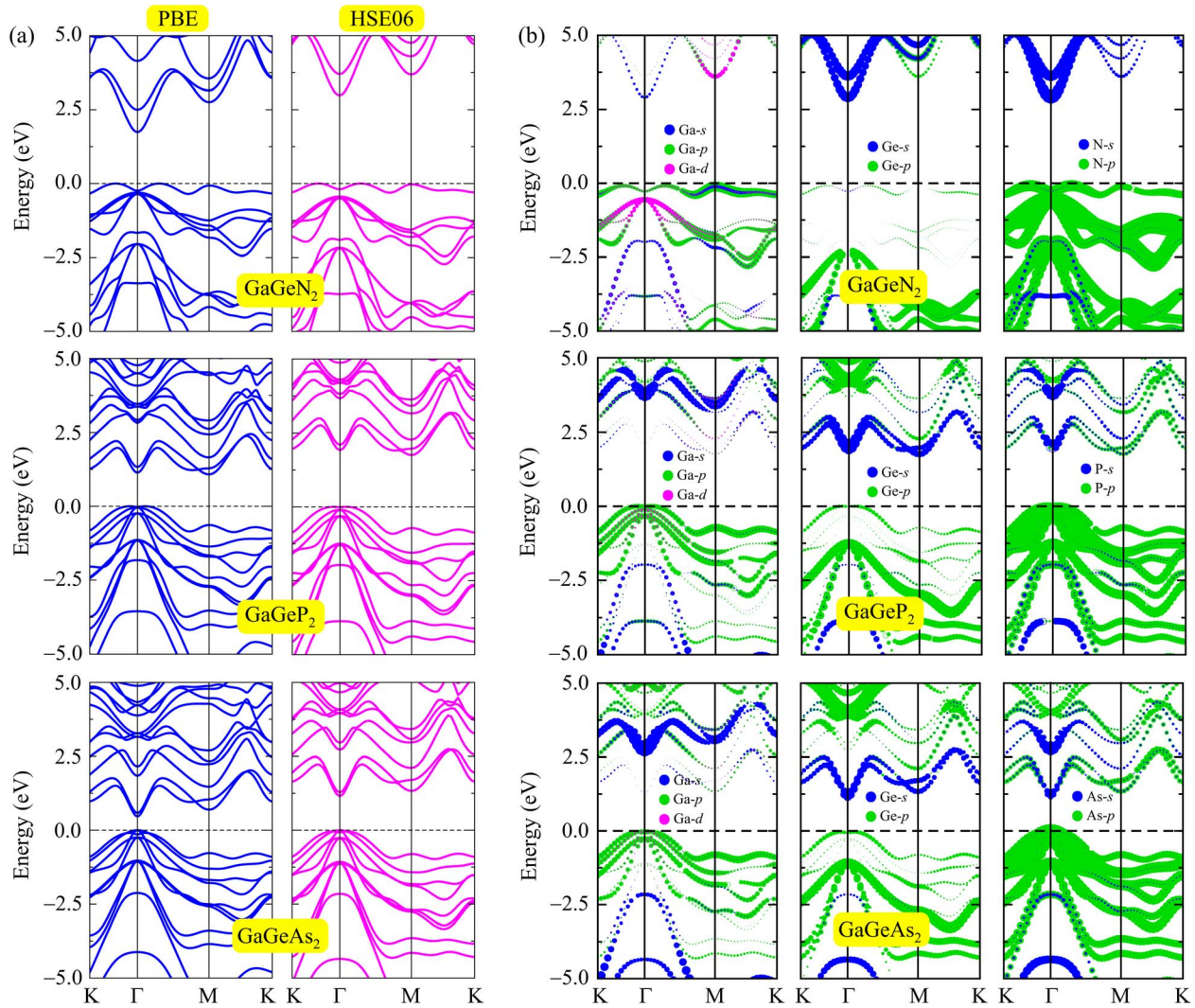

Fig. 4 (a) Electronic band structures at PBE/HSE06 levels and (b) weighted band structures of $GaGeN_2$, $GaGeP_2$, and $GaGeAs_2$ monolayers with the Fermi level indicated by the dashed horizontal line at zero.

$GaGeN_2$, 1.75 eV for $GaGeP_2$ and 1.15 eV for $GaGeAs_2$ monolayer. The bandgap values of the $GaGeP_2$ and $GaGeAs_2$ are optimal for absorption in the visible spectrum, suggesting the potential application of these monolayers in photovoltaic devices. Additionally, we calculate the bandgap energy with the presence of spin–orbit coupling (SOC), since this SOC interaction has significant influences on the electronic band structure of the materials. The HSE06+SOC band structures and corresponding partial density of states (PDOS) of $GaGeX_2$ monolayers are depicted in Fig. 5. It is found that the influence of SOC on the electronic bands of $GaGeX_2$ monolayers is quite weak. When SOC is taken into account, the spin degeneracy is eliminated, however, as depicted in Fig. 5, the spin-splitting energy is insignificant. At the HSE06+SOC band gaps of $GaGeN_2$, $GaGeP_2$, and $GaGeAs_2$ are found to be 2.89, 1.70, and 1.04 eV, respectively, as presented in Table 1. Thus, the bandgap of the studied materials is only reduced very slightly when SOC is included.

The weighted band structures of the $GaGeX_2$ systems are also performed to elucidate the contribution of elements to the formation of electronic bands. As shown in Fig. 4(b), the $GaGeP_2$ and $GaGeAs_2$ monolayers have quite similar weighted band structures. In general, the p orbitals of Ga, Ge, and X atoms have strong contributions to the valence band. Especially, the valence band maximum (VBM) near the Fermi level is mainly contributed by the X-p orbitals. The Ga-s, Ge-s, and X-s orbitals also give small contributions to the valence band at low-energy regions. Meanwhile, these s orbitals of Ga, Ge, and X atoms significantly contribute to the formation of conduction band minimum (CBM). The Ge-p and X-p orbitals have weaker contributions to the conduction band of the $GaGeP_2$ and $GaGeAs_2$ monolayers at high energy regions. The contribution of Ga-d orbitals to both the formation of valence and conduction bands is quite small compared with other orbitals.

Next, we determine another important characteristic of the electrons, the work function Φ, which can evaluate the potential for electrons to leave the surface of materials. Based on the calculation of electrostatic potentials, Φ is estimated from the vacuum level (E_{vac}) and Fermi level (E_F) by following equation:

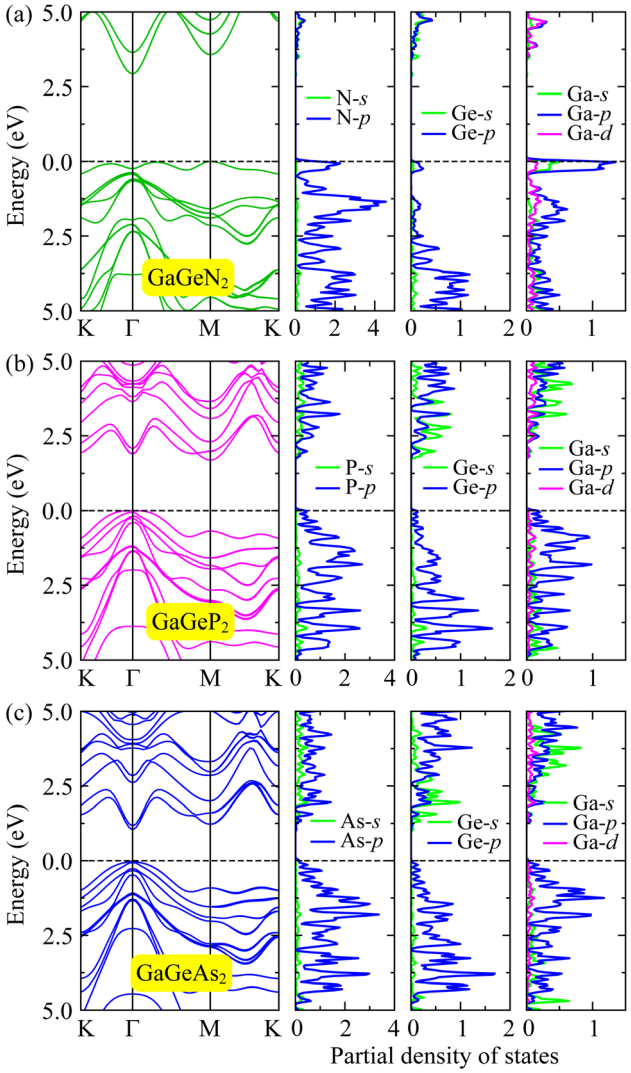

Fig. 5 Calculated HSE06 + SOC band structures and corresponding partial density of states of $GaGeN_2$ (a), $GaGeP_2$ (b), and $GaGeAs_2$ (c) monolayers.

$$\Phi = E_{vac} - E_F. \quad (8)$$

Fig. 6 illustrates the planar electrostatic potentials of the $GaGeX_2$ monolayers. It can be observed the decrease of work function when the X atom transfers from N to P/As. The $GaGeN_2$ has a higher work function than that of the $GaGeP_2$ and $GaGeAs_2$ structures. This indicates that the electrons can escape from the surface of $GaGeP_2$ and $GaGeAs_2$ more easily than the $GaGeN_2$ surface. The obtained work function values vary from 4.79 eV for $GaGeAs_2$ to 6.31 eV for $GaGeN_2$ as summarized in Table 1.

3.5 Transport properties

To evaluate the applicability for electronic applications of the materials, we examine the transport properties of the $GaGeX_2$ monolayers. An important factor directly related to the charge transport is the carrier mobilities μ_{2D}, which can be determined by using the DP approximation as the following:[32,45]

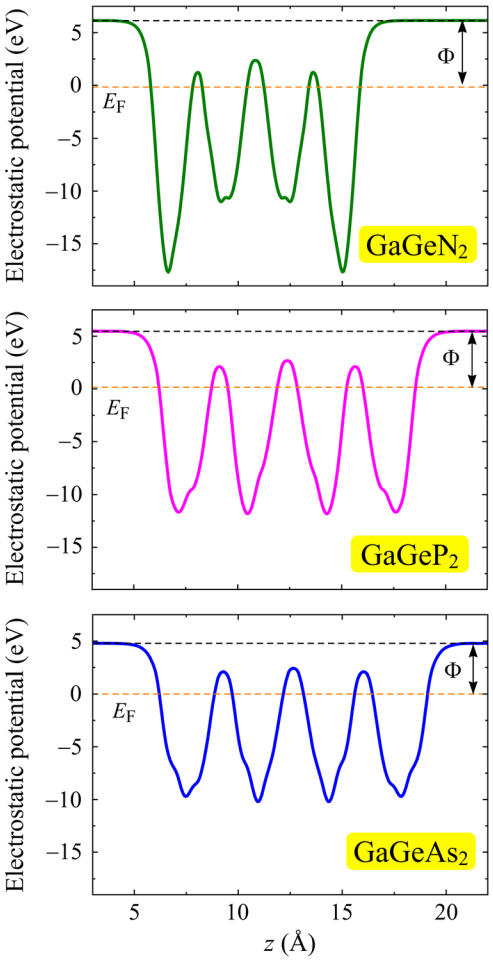

Fig. 6 Electrostatic potential of $GaGeX_2$ monolayers with the dipole correction. The dashed orange lines indicate the Fermi level.

$$\mu_{2D} = \frac{e\hbar^3 C_{2D}}{k_B T m^* \overline{m} E_d^2}, \quad (9)$$

with $\hbar$ and k_B correspond to the reduced Planck and Boltzmann constants, respectively. e indicates the elementary charge and T is the chosen temperature (300 K). m^* and $\overline{m} = \sqrt{m_x^* m_y^*}$ refer to the carrier effective mass and average effective mass, respectively. E_d relates to the DP constant and C_{2D} is the elastic modulus.

Thus to estimate the carrier mobilities μ_{2D}, we have to find the carrier effective mass m^*, the elastic modulus C_{2D}, and the DP constant E_d. Among these parameters, the C_{2D} can be expressed as:

$$C_{2D} = \frac{1}{\Omega_0} \frac{\partial^2 E_{tot}}{\partial \varepsilon_{uni}^2}, \quad (10)$$

where ε_{uni} is the uniaxial strain in x and y transport directions. Ω_0 indicates the optimized unit-cell area. E_{tot} corresponds to the total energy. The DP constant E_d is evaluated by using the following expressions:

$$E_d = \frac{\Delta E_{edge}}{\varepsilon_{uni}}, \quad (11)$$

where ΔE_{edge} relates to the energy variation of the band edges.

The uniaxial strain ($\varepsilon_{uni}^{x/y}$) is added along the x and y axes, with a range of −1 to 1%, for the calculations. The values of C_{2D} and E_d can be achieved by fitting the dependence of applied strain with energy and band edges.[44,45] Fig. 7 depicts the changing energy and positions of band edges of the $GaGeX_2$ monolayers. We can observe that the C_{2D} of all three structures is directional isotropic. The calculated C_{2D} values are almost the same between the two different x and y directions as listed in Table 3. Besides, the band edge positions of the $GaGeN_2$, $GaGeP_2$, and $GaGeAs_2$ monolayers along the two in-plane directions are almost the same. The $GaGeX_2$ monolayers show anisotropic DP constants along the transport directions with the E_d values ranging from −15.59 to −4.77 eV. Some other Janus materials are also found to have the anisotropic DP constant such as Ga_2Te_3,[46] $STiSiAs_2$,[47] and Ga_2SX_2.[16] This anisotropic E_d can lead to the anisotropy of carrier mobility of the $GaGeX_2$ monolayers.

The carrier effective mass m^*, which has a significant impact on the mobility of carriers, can be derived as follows:

$$\frac{1}{m^*} = \frac{1}{\hbar^2}\left|\frac{\partial^2 E(k)}{\partial k^2}\right|, \quad (12)$$

where $E(k)$ stands for the energy of the wave-vector k at the band edges. From this equation, the $\partial^2 E(k)/\partial k^2$ is small if the band diagram around the band edges is flat, resulting in a high effective mass. Table 3 summarizes the obtained m^* values. The effective masses along the x and y directions of electrons are quite small ranging from 0.09 to $0.41m_0$. Meanwhile, the $GaGeP_2$ monolayer exhibits the highest hole effective mass m_h^* in the x direction of $7.74m_0$. In general, the effective masses of holes for the three monolayers are higher than the effective masses of electrons. This is in good agreement with the flatter band diagram around the valence band edge compared with the conduction band edge as presented in Fig. 4(a). The high hole effective masses may lead to low hole mobilities due to their slow response to the external electric field.

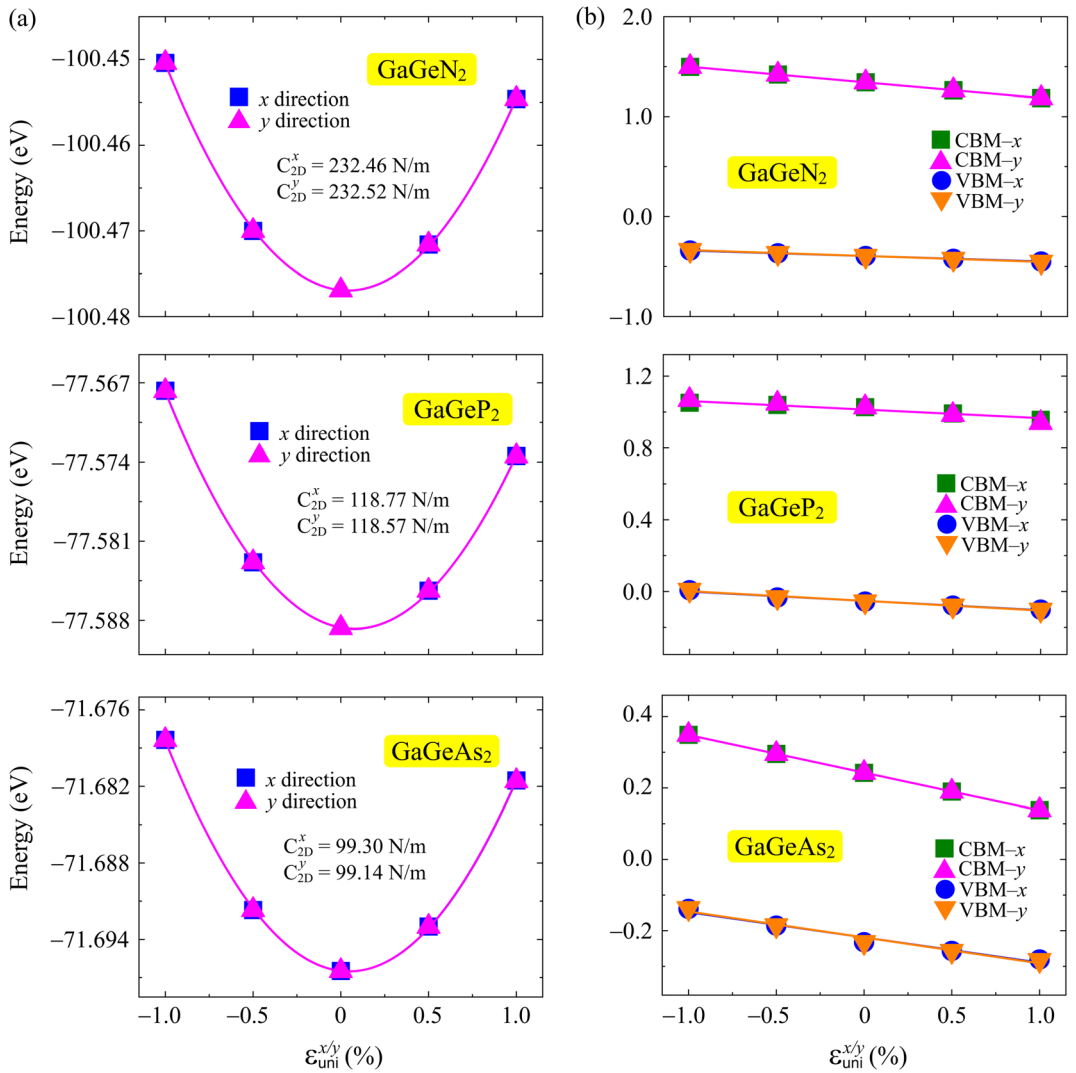

Fig. 7 The total energy (a) and band edges (b) dependence on applied strains in the x/y directions of $GaGeX_2$ systems. The fitted curves are indicated by the solid lines.

Table 3 Effective masses of carriers m^* (in mass of free electron unit m_0), 2D elastic modulus C_{2D} (N m^{-1}), DP constants E_d (eV), and mobility of carriers μ (cm^2 V^{-1} s^{-1}) of $GaGeX_2$ materials along the two in-plane axes

		m_x^*	m_y^*	$C_{2D}{}^x$	$C_{2D}{}^y$	$E_d{}^x$	$E_d{}^y$	μ_x	μ_y
Electron	$GaGeN_2$	0.21	0.23	232.46	232.52	−15.59	−15.59	447.33	415.23
	$GaGeP_2$	0.41	0.30	118.77	118.57	−4.77	−6.39	776.95	578.63
	$GaGeAs_2$	0.09	0.11	99.30	99.14	−10.55	−10.54	2270.17	1788.59
Hole	$GaGeN_2$	4.70	1.73	232.46	232.52	−5.51	−5.85	12.19	29.41
	$GaGeP_2$	7.74	1.38	118.77	118.57	−5.23	−5.40	3.65	19.24
	$GaGeAs_2$	0.77	0.68	99.30	99.14	−7.10	−7.27	75.06	80.38

According to the obtained parameters of E_d, C_{2D}, and m^*, we can find the values of carrier mobilities μ_{2D} by using eqn (9). The calculated carrier mobilities of all three monolayers are listed in Table 3. The μ_{2D} values of the $GaGeX_2$ are anisotropic in the two in-plane directions for both electrons and holes. As expected from the effective mass results, the electron mobilities of all three $GaGeX_2$ monolayers are higher than the hole mobilities. In particular, the $GaGeN_2$ and $GaGeP_2$ structures have quite low hole mobilities of 3.65 to 29.41 cm^2 V^{-1} s^{-1} for both the two in-plane directions, while the $GaGeAs_2$ monolayer exhibits the highest electron mobilities of 2270.17 and 1788.59 cm^2 V^{-1} s^{-1} for the x and y directions, respectively. The $GaGeN_2$ and $GaGeP_2$ show lower electron mobilities of 447.33 and 776.95 cm^2 V^{-1} s^{-1} in the x direction, respectively. The obtained electron mobility of the $GaGeAs_2$ monolayer is higher than that of the other reported Janus materials of Ga_2SSe_2,[16] In_2SeO,[17] $MoSiAs_3H$,[19] and $WSiAs_3H$.[39] The anisotropic and high electron mobility of the $GaGeAs_2$ monolayer shows potential applications of this material in the electronic fields.

4 Conclusion

In summary, we have conducted first-principles calculations to examine the crystal structures and physical characteristics of the $GaGeX_2$ monolayers. Our analyses of the cohesive energy, phonon dispersion spectra, and AIMD simulations demonstrate that the three proposed structures have good energetic, dynamic, and thermodynamic stabilities. The Raman spectra are performed for the Raman activities and vibrational properties of the $GaGeX_2$ systems. From the calculated piezoelectric coefficients, the $GaGeX_2$ are found as piezoelectric materials with the high d_{11} of −1.23 pm V^{-1} for the $GaGeAs_2$ monolayer. Our PBE and HSE06 investigations reveal that the $GaGeX_2$ are semiconductors with moderate bandgap energies. At the HSE06 level, the $GaGeP_2$ and $GaGeAs_2$ structures exhibit optimal bandgaps for photovoltaic applications of 1.75 and 1.15 eV, respectively. Moreover, all three investigated $GaGeX_2$ systems have anisotropic carrier mobility in the two in-plane directions for both electrons and holes. Among them, the $GaGeAs_2$ monolayer shows the highest electron mobilities of 2270.17 and 1788.59 cm^2 V^{-1} s^{-1} for the x and y directions, respectively. With high electron mobility, large piezoelectric coefficient, and optimal bandgap energy, the $GaGeAs_2$ material holds potential applicability for applications in multifunctional devices.

Data availability

All data that support the findings of this study are included within the article.

Conflicts of interest

There are no conflicts of interest to declare.

References

1 H. Zhao, Y. Gu, N. Lu, Y. Liu, Y. Ding, B. Ye, X. Huo, B. Bian, C. Wei, X. Zhang and G. Yang, *Chem. Phys.*, 2022, **553**, 111384.
2 V. D. Dat and T. V. Vu, *New J. Chem.*, 2022, **46**, 1557–1568.
3 M. Dragoman, A. Dinescu and D. Dragoman, *Phys. Status Solidi A*, 2019, **216**, 1800724.
4 Z. Liu, H. Wang, J. Sun, R. Sun, Z. F. Wang and J. Yang, *Nanoscale*, 2018, **10**, 16169–16177.
5 F. R. Fan, R. Wang, H. Zhang and W. Wu, *Chem. Soc. Rev.*, 2021, **50**, 10983–11031.
6 Y. Zhu, L. Peng, Z. Fang, C. Yan, X. Zhang and G. Yu, *Adv. Mater.*, 2018, **30**, 1706347.
7 T. Tan, X. Jiang, C. Wang, B. Yao and H. Zhang, *Adv. Sci.*, 2020, **7**, 2000058.
8 H. Zhu, Y. Wang, J. Xiao, M. Liu, S. Xiong, Z. J. Wong, Z. Ye, Y. Ye, X. Yin and X. Zhang, *Nat. Nanotechnol.*, 2014, **10**, 151–155.
9 C. Zhang, Y. Nie, S. Sanvito and A. Du, *Nano Lett.*, 2019, **19**, 1366–1370.
10 M. Tahir, N. Fatima, U. Fatima and M. Sagir, *Inorg. Chem. Commun.*, 2021, **124**, 108242.
11 X. Liu, S. Zhang, S. Guo, B. Cai, S. A. Yang, F. Shan, M. Pumera and H. Zeng, *Chem. Soc. Rev.*, 2020, **49**, 263–285.
12 N. K. Chaudhari, H. Jin, B. Kim, D. San Baek, S. H. Joo and K. Lee, *J. Mater. Chem. A*, 2017, **5**, 24564–24579.
13 C.-H. Lai, M.-Y. Lu and L.-J. Chen, *J. Mater. Chem.*, 2012, **22**, 19–30.
14 T. Kajana, A. Pirashanthan, D. Velauthapillai, A. Yuvapragasam, S. Yohi, P. Ravirajan and M. Senthilnanthanan, *RSC Adv.*, 2022, **12**, 18041–18062.
15 M. Bikerouin, O. Chdil and M. Balli, *Nanoscale*, 2023, **15**, 7126–7138.
16 N. N. Hieu, H. V. Phuc, A. I. Kartamyshev and T. V. Vu, *Phys. Rev. B*, 2022, **105**, 075402.

17 T. V. Vu, C. V. Nguyen, H. V. Phuc, A. A. Lavrentyev, O. Y. Khyzhun, N. V. Hieu, M. M. Obeid, D. P. Rai, H. D. Tong and N. N. Hieu, *Phys. Rev. B*, 2021, **103**, 085422.
18 I. Bouziani, M. Kibbou, Z. Haman, N. Khossossi, I. Essaoudi, A. Ainane and R. Ahuja, *Phys. E*, 2021, **134**, 114900.
19 X. Cai, G. Chen, R. Li, W. Yu, X. Yang and Y. Jia, *Phys. Chem. Chem. Phys.*, 2023, **25**, 29594–29602.
20 J. Wang, H. Guo, J. Xue, D. Chen, G. Yang, B. Liu, H. Lu, R. Zhang and Y. Zheng, *Sol. RRL*, 2019, **3**, 1900321.
21 L. Dong, J. Lou and V. B. Shenoy, *ACS Nano*, 2017, **11**, 8242–8248.
22 Y. Cui, L. Peng, L. Sun, M. Li, X. Zhang and Y. Huang, *J. Phys.: Condens.Matter*, 2019, **32**, 08LT01.
23 G. Kresse and J. Furthmüller, *Phys. Rev. B: Condens. Matter Mater. Phys.*, 1996, **54**, 11169–11186.
24 G. Kresse and J. Furthmüller, *Comput. Mater. Sci.*, 1996, **6**, 15–50.
25 P. E. Blöchl, *Phys. Rev. B: Condens. Matter Mater. Phys.*, 1994, **50**, 17953.
26 G. Kresse and D. Joubert, *Phys. Rev. B: Condens. Matter Mater. Phys.*, 1999, **59**, 1758–1775.
27 J. P. Perdew, K. Burke and M. Ernzerhof, *Phys. Rev. Lett.*, 1996, **77**, 3865.
28 A. Togo, L. Chaput and I. Tanaka, *Phys. Rev. B: Condens. Matter Mater. Phys.*, 2015, **91**, 094306.
29 J. Heyd, G. E. Scuseria and M. Ernzerhof, *J. Chem. Phys.*, 2003, **118**, 8207.
30 S. Grimme, J. Antony, S. Ehrlich and H. Krieg, *J. Chem. Phys.*, 2010, **132**, 154104.
31 M. Yagmurcukardes, F. M. Peeters and H. Sahin, *Phys. Rev. B*, 2018, **98**, 085431.
32 J. Bardeen and W. Shockley, *Phys. Rev.*, 1950, **80**, 72.
33 T. V. Vu, V. T. T. Vi, N. T. Hiep, K. V. Hoang, A. I. Kartamyshev, H. V. Phuc and N. N. Hieu, *RSC Adv.*, 2024, **14**, 21982–21990.
34 K.-A. N. Duerloo, M. T. Ong and E. J. Reed, *J. Phys. Chem. Lett.*, 2012, **3**, 2871–2876.
35 R. C. Andrew, R. E. Mapasha, A. M. Ukpong and N. Chetty, *Phys. Rev. B: Condens. Matter Mater. Phys.*, 2012, **85**, 125428.
36 N. T. Hung, A. R. T. Nugraha and R. Saito, *J. Phys. D: Appl. Phys.*, 2018, **51**, 075306.
37 N. T. Hiep, C. Q. Nguyen, N. A. Poklonski, C. A. Duque, H. V. Phuc, D. V. Lu and N. N. Hieu, *J. Phys. D: Appl. Phys.*, 2023, **56**, 385306.
38 Y. Liu, C. Shao, W. Yu, Q. Gui, J. Robertson and Y. Guo, *Appl. Phys. Lett.*, 2022, **121**, 244105.
39 T. V. Vu, B. D. Hoi, A. I. Kartamyshev and N. N. Hieu, *J. Appl. Phys.*, 2024, **135**, 074301.
40 V. T. T. Vi, T. P. T. Linh, C. Q. Nguyen and N. N. Hieu, *Adv. Theory Simul.*, 2022, **5**, 2200499.
41 Y. Guo, S. Zhou, Y. Bai and J. Zhao, *Appl. Phys. Lett.*, 2017, **110**, 163102.
42 M. T. Ong and E. J. Reed, *ACS Nano*, 2012, **6**, 1387–1394.
43 H.-N. Zhang, Y. Wu, C. Yang, L.-H. Zhu and X.-C. Wang, *Phys. Rev. B*, 2021, **104**, 235437.
44 S.-D. Guo, W.-Q. Mu, Y.-T. Zhu, R.-Y. Han and W.-C. Ren, *J. Mater. Chem. C*, 2021, **9**, 2464–2473.
45 W. Wan, S. Zhao, Y. Ge and Y. Liu, *J. Phys.: Condens.Matter*, 2019, **31**, 435501.
46 C.-F. Fu, J. Sun, Q. Luo, X. Li, W. Hu and J. Yang, *Nano Lett.*, 2018, **18**, 6312–6317.
47 Z. Gao, X. He, W. Li, Y. He and K. Xiong, *Dalton Trans.*, 2023, **52**, 8322–8331.